PAPER

Enhanced multimaterial 4D printing with active hinges

IOP Publishing Smart Materials and Structures
Smart Mater. Struct. 27 (2018) 065027 (15pp) https://doi.org/10.1088/1361-665X/aabe63

Enhanced multimaterial 4D printing with active hinges

Saeed Akbari[1], Amir Hosein Sakhaei[1], Kavin Kowsari[1], Bill Yang[1], Ahmad Serjouei[1], Zhang Yuanfang[1] and Qi Ge[1,2]

[1] Digital Manufacturing and Design Center, Singapore University of Technology and Design, Singapore 487372, Singapore
[2] Science and Math Cluster, Singapore University of Technology and Design, Singapore 487372, Singapore

E-mail: ge_qi@sutd.edu.sg

Received 30 January 2018, revised 21 March 2018
Accepted for publication 16 April 2018
Published 9 May 2018

Abstract

Despite great progress in four-dimensional (4D) printing, i.e. three-dimensional (3D) printing of active (stimuli-responsive) materials, the relatively low actuation force of the 4D printed structures often impedes their engineering applications. In this study, we use multimaterial inkjet 3D printing technology to fabricate shape memory structures, including a morphing wing flap and a deployable structure, which consist of active and flexible hinges joining rigid (non-active) parts. The active hinges, printed from a shape memory polymer (SMP), lock the structure into a second temporary shape during a thermomechanical programming process, while the flexible hinges, printed from an elastomer, effectively increase the actuation force and the load-bearing capacity of the printed structure as reflected in the recovery ratio. A broad range of mechanical properties such as modulus and failure strain can be achieved for both active and flexible hinges by varying the composition of the two base materials, i.e. the SMP and the elastomer, to accommodate large deformation induced during programming step, and enhance the recovery in the actuating step. To find the important design parameters, including local deformation, shape fixity and recovery ratio, we conduct high fidelity finite element simulations, which are able to accurately predict the nonlinear deformation of the printed structures. In addition, a coupled thermal-electrical finite element analysis was performed to model the heat transfer within the active hinges during the localized Joule heating process. The model predictions showed good agreement with the measured temperature data and were used to find the major parameters affecting temperature distribution including the applied voltage and the convection rate.

Supplementary material for this article is available online

Keywords: 4D printing, shape memory polymer, enhanced recovery, finite element modeling

(Some figures may appear in colour only in the online journal)

1. Introduction

Three-dimensional (3D) printing, also known as additive manufacturing, has been widely adopted in different industries owing to its powerful capability for rapid fabrication of complex 3D structures for a wide variety of applications [1–3]. 3D printing technologies have been increasingly used to create mechanism components for robots, flight vehicles, and other applications [4–7]. However, to date, the motions of these mechanisms are only driven by the external actuators (i.e. traditional motors). Integrating these chunky and often heavy motors into printed mechanism components significantly increases the manufacturing complexity and limits the design flexibility. Therefore, developing a novel approach based on 3D printing to combine mechanisms and actuators as a single unity is highly desired.

The emerging 4D printing technology [8–16], which adds a fourth dimension 'time' to 3D printed structures, offers a practical solution to integrating actuation into printed mechanisms. Based on previous reports, 4D printing is

realized by 3D printing structures with soft active materials (SAMs) which exhibit large deformation in response to environmental stimuli such as heat, moisture, voltage, magnetic field, and others. Among the existing SAMs, the thermally-responsive shape memory polymers (SMPs) are regarded as one of the most promising candidates for 4D printing, due to their compatibility with 3D printing, relatively large recovery force and fast responding rate [3, 14–20]. In recent years, many efforts have been made to demonstrate 4D printing using thermal responsive SMPs. Examples include self-assembly coiling, twisting and wavy-shape strips [9], sequential recovering structures [18], and active origami [15]. However, in these demonstrations, the 4D printed structures became soft when the free recovery was triggered at high temperatures, as the SMPs entered the low stiffness rubbery state. This low stiffness in free recovery process significantly impedes the application of the 4D printed parts to practical engineering structures. In addition, the thermal actuation of the 4D printed SMP structures in previous studies was mostly triggered through the change of ambient temperature by placing the printed structures into hot water or thermal chambers, which cannot be used for real applications that require precise and timely control of temperature.

In this study, to address the abovementioned two challenges, we report a design and fabrication methodology for enhanced multimaterial 4D printing, in which SMP active hinges are produced using a high-resolution, multimaterial inkjet 3D printing technology. The recovery force is enhanced by combining the active hinges with the elastic flexible hinges which store elastic strain energy during programming, then release it during actuation to increase the recovery force. To demonstrate the enhancements, we 4D printed two different structures: a morphing wing flap and a deployable structure. We also introduce a method by embedding resistive wires into the printed structures to realize localized Joule heating. Optimal actuation parameters such as actuation voltage were determined using a coupled thermal-electrical finite element analysis (FEA) to predict temperature distribution in the active hinges during Joule heating. We also performed finite element simulations using user material subroutine (UMAT) based on a multi-branch viscoelastic model to accurately simulate the shape memory behavior of the 4D printed structures.

2. Materials and methods

2.1. Design of 4D printed structures

A common method to increase recovery force of SMPs is to increase their stiffness through the addition of reinforcements such as carbon fibers [21–23] or silicon carbide nano-particles [24]. This technique, however, greatly increases fabrication time and requires additional manufacturing steps and may negatively influence the shape memory behavior. In this paper, we propose an alternative approach by designing and 3D printing actuators consisting of active hinges reinforced by elastic flexible hinges to increase the recovery force.

As schematically shown in figure 1, we demonstrate the approach using two representative structures: a morphing wing flap (figures 1(a), (b)) that exhibits large bending deformation, and a deployable structure that exhibits large extensional deformation (figures 1(c), (d)). The wing flap consisted of two active hinges and one flexible hinge and was initially manufactured in a bent shape (figure 1(a)). Following a thermomechanical process, the bent wing flap was programmed into a temporary straight shape. The programming and actuating were performed using localized Joule heating by applying current to the resistant wires that were embedded into the active hinges as discussed in section 2.3. Similarly, localized Joule heating was used to trigger the free expansion of the deployable structure (figures 1(c), (d)), which was initially manufactured in a standing 3D shape, then programmed into a compact, nearly 2D shape. The thickness of all hinges in both structures was 3 mm.

2.2. Characterization of printed materials

Programming and actuating the 4D printed structures are performed at the temperatures which are related to the glass transition temperature (T_g) of the SMPs used to print the active hinges. Also, the allowable strains of the 3D printing materials used to fabricate the active and flexible hinges must be sufficient to accommodate the large deformation induced during programming and actuating steps. In addition, the stiffness of the flexible hinges must be sufficient to deliver the desired recovery force and increase the load-bearing capacity of the structure. In order to measure the thermomechanical properties of the printing materials used in this study, a series of characterization tests were performed, which are explained in sections 2.2.1 and 2.2.2.

2.2.1. Dynamic mechanical analysis. A dynamic mechanical analysis (DMA) tester (Q800 DMA, TA Instruments, New Castle, DE, USA) was used to measure thermomechanical properties of the base materials, VeroClear and Agilus30 (Stratasys Ltd, Eden Prairie, MN, USA), as well as eight digital materials which are the mixtures of the two base materials. The rectangular samples with dimensions of 15 mm × 5 mm × 1 mm were dynamically strained at a frequency of 1 Hz with a peak-to-peak amplitude of 0.1%. Each sample was first equilibrated at a temperature at least 30 °C higher than its glass transition temperature (T_g) for 10 min, then cooled down to a low temperature at which the sample was at its glassy state.

Figures 2(a), (b) show the changes with temperature of storage modulus and Tanδ for different printing materials. The T_gs of the tested materials were identified as the temperature where Tanδ reaches the maximum, and plotted in figure 2(c). We conclude that three of the tested materials, including RGD8630, RGD8625, and VeroClear, potentially exhibit shape memory behavior, since their T_gs are higher than room temperature, and they transit from the glassy state to the rubbery state when heated from room temperature to a

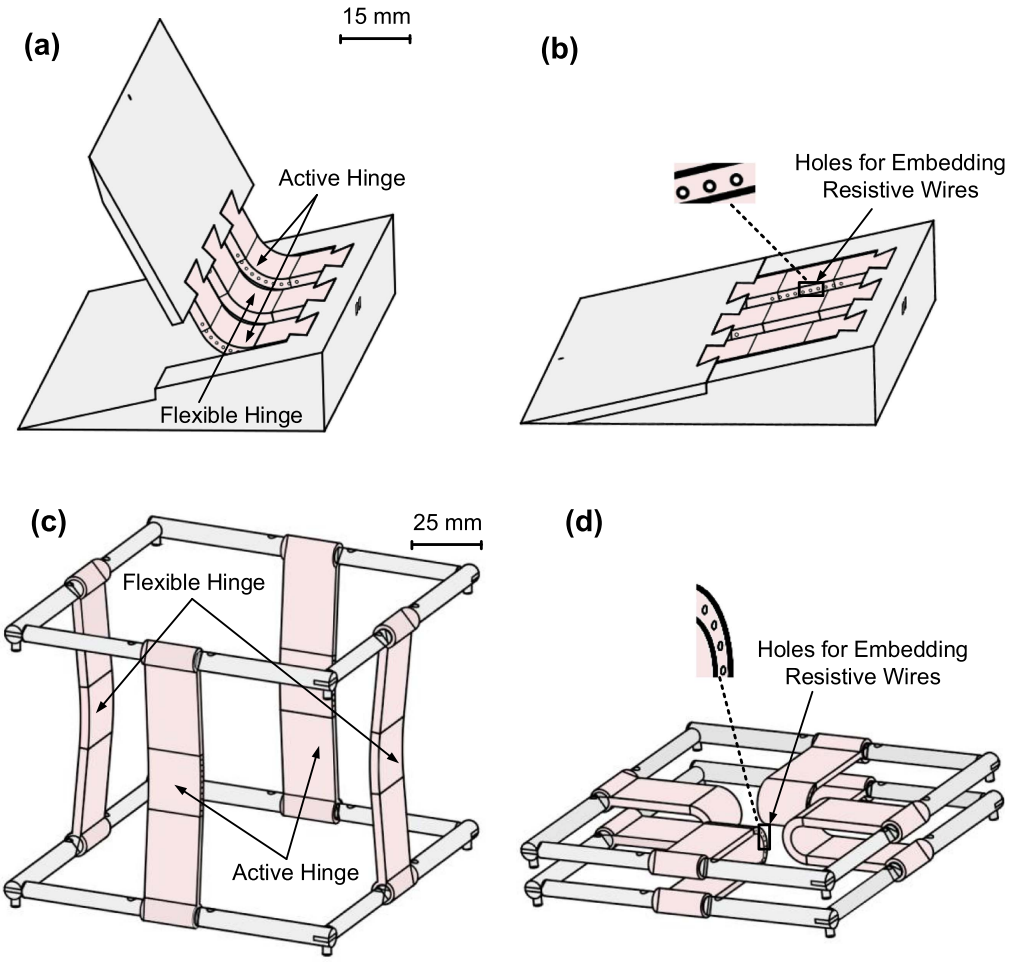

Figure 1. Schematic of the 4D printed shape memory structures with active and flexible hinges. (a) As-printed morphing wing flap consisting of three hinges, including two active hinges and one flexible hinge. (b) Programmed shape of the morphing wing flap after thermomechanical training. (c) As-printed deployable structure with four hinges, including two active hinges and two flexible hinges. (d) Programmed shape of the deployable structure after thermomechanical training.

temperature higher than T_g. Based on these findings, we select VeroClear ($T_g = 58\,^{\circ}C$) to print the active hinges as it has the highest rubbery modulus, and thus the highest recovery stress.

2.2.2. Uniaxial tensile tests. In order to better understand the mechanical behavior of 3D printing materials used in this study, and to determine the material parameters required in the simulation of the active and flexible hinges, we performed a series of uniaxial tensile tests at different temperatures. Following ASTM D638-10 test standard for tensile testing of plastics, three samples of each polymer were tested using a universal testing machine (Criterion Model 43, MTS Systems Corporation, Eden Prairie, MN, USA) equipped with a thermal chamber and a video extensometer. The strains were measured using the digital image correlation technology. The tensile samples were loaded at a testing speed of 2 mm min^{-1} until fracture.

Figure 3(a) presents the stress–strain behavior of VeroClear tested at different temperatures. Consistent with previous studies on polymers characterization, the stress–strain behavior shows a high temperature dependency [25–27]. From 25 °C to 40 °C, VeroClear exhibits an elastoplastic behavior, and its maximum elastic strain is less than the failure strain (strain at the moment of fracture). Also, at this temperature range, the Young's modulus gradually decreases with the increase of the testing temperature (figure 3(b)). Once the testing temperature reaches 50 °C or higher, VeroClear exhibits linear elastic behavior.

Moreover, as the 4D printed active hinges undergo a large deformation during programming and actuating at temperatures higher than T_g, it is important to understand the effect of temperature on the failure strain of VeroClear. Figure 3(b) presents the temperature dependant failure strains of VeroClear which were extracted from figure 3(a). The failure strain of VeroClear changes rapidly with temperature. It starts from 25% at $T = 25\,^{\circ}C$, increases with temperature, and reaches a maximum value 59% at $T = 35\,^{\circ}C$. Then, it decreases continuously and reaches 26% at $T = 80\,^{\circ}C$ and a minimum of 19% at $T = 90\,^{\circ}C$.

Joule heating is used to heat the active hinges printed from VeroClear, while the flexible hinges printed from the elastomeric digital materials always remain in the room temperature. Therefore, we also tested the stress–strain behavior at room temperature for the candidate elastomeric

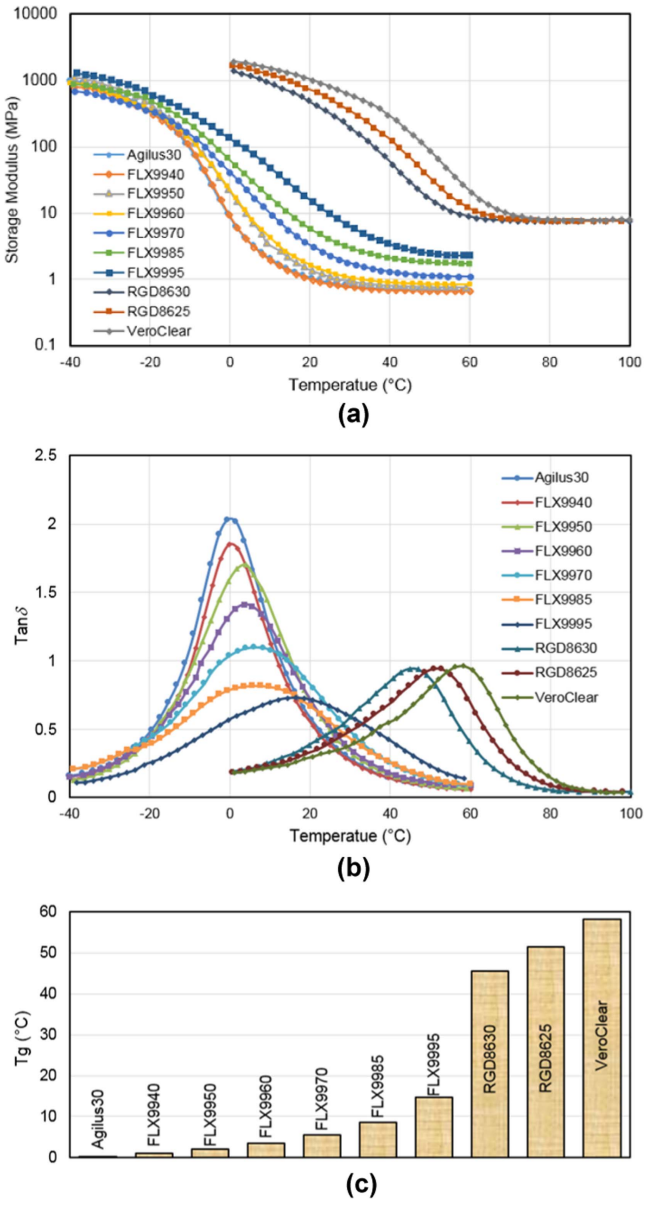

Figure 2. Results of DMA tests of ten different printing materials. (a) Storage modulus versus temperature. (b) Tanδ versus temperature. (c) T_gs of printing materials.

digital materials including the base elastomer, Agilus30, and the mixtures of Agilus30 and VeroClear (denoted with the prefix FLX in their names). As the T_gs of all the elastomers are below the room temperature, they exhibit an elastic stress–strain behavior with a large failure strain and a low tensile strength. With increase of VeroClear concentration (the notations of the elastomers vary from Agilus30 to FLX9995), an increase in the tensile strength (from 0.7 to 4.2 MPa) and a decrease in the failure strain (from 175% to 53%) are observed. The Young's modulus of these materials, which were used to print the flexible hinges of the 4D printed structures, was measured at 1% strain of the stress–strain curve, as shown in figure 3(d). A flexible hinge printed with a stiffer material can store a higher elastic strain energy during programming and generate a higher recovery force in actuation. On the other hand, stiffer elastomers have a lower failure strain, which restricts their deformability in programming step. We use a finite element model, described in section 3.2, to find the maximum strain in the deformed hinges, and ensure it is lower than the failure strain of the digital materials used to print the flexible hinge.

2.3. Fabrication of the 4D printed structures

Both active structures, the morphing wing flap (figures 1(a), (b)) and the deployable structure (figures 1(c), (d)), were first 3D printed, and then assembled to the configurations shown in figure 4. The as-fabricated morphing wing flap (figure 4(a)) was assembled from moving and stationary rigid parts connected using three hinges, including two active hinges and one flexible hinge. The rigid parts (moving flap part and stationary part) were produced using a fused deposition modeling printer (Fortus 450MC, Stratasys Ltd) from a high-performance thermoplastic, acrylic-styrene-acrylonitrile, whereas both the active and flexible hinges were fabricated using an inkjet multimaterial 3D printer (Objet500 Connex 3, Stratasys Ltd). As described in section 2.2.1, the active hinges were printed using the base material VeroClear which has the shape memory effect. For the flexible hinge, the middle section was printed with an elastic digital material (properties of figures 3(c), (d)), and the two end sections were printed with the rigid VeroClear, and later used to connect the flap moving and stationary parts.

A similar procedure was followed to fabricate the deployable structure (figures 1(c), (d) and 4(b)), which was comprised of eight rigid rods, two active hinges and two flexible hinges. All parts were printed in a single printing job using the multimaterial inkjet printer, and then assembled together to create the deployable structure. It is important to note that using the one-step inkjet 3D printing process considerably reduced the fabrication time and complexity, otherwise not possible with traditional manufacturing methods based on molding and casting.

Localized Joule heating, which precisely controls the free recovery of active hinges in both structures of figure 4, was achieved using resistive wires (Constantan, copper–nickel alloy) with a resistance of $3.90\,\Omega\,m^{-1}$ and diameter of 0.4 mm, which were embedded into the equally-spaced holes designed for each active hinge. The programming and actuating temperatures of the active hinges were assumed to be 68 °C, which is 10 °C higher than the T_g of VeroClear (figure 2(c)). The coupled thermal-electrical finite element simulations presented in section 3.1 suggest that this temperature can be achieved by applying a unit voltage of $12.7\,V\,m^{-1}$ (volts per unit length of the resistive wire) for 15 s, which corresponds to the application of 3.3 A electrical current. The two active hinges in each 4D printed structure were connected in series to ensure the electrical current, and hence the temperature, is identical in both hinges. Temperature measurement using an infrared thermometer camera (Fluke 297 FC, Fluke Co., Everett, WS, USA) confirmed that the maximum temperature difference between the two connected active hinges during programming was always less than 2 °C.

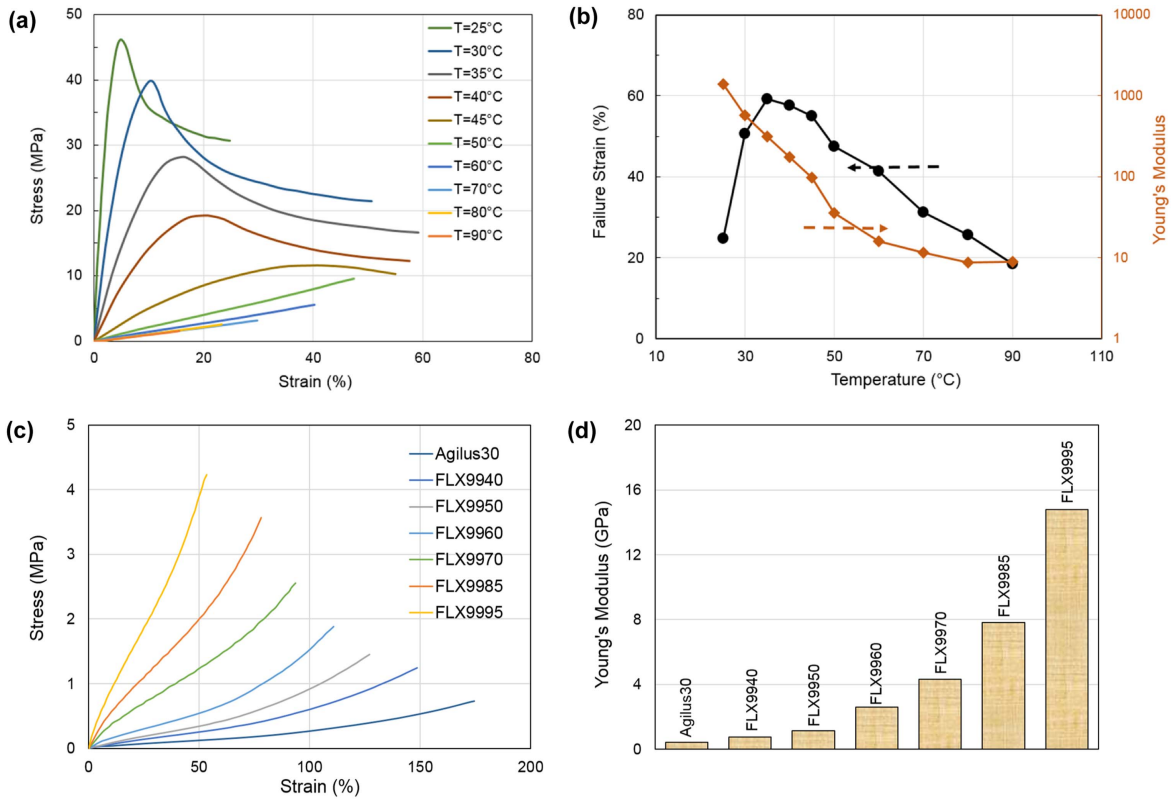

Figure 3. Tensile test results of the printing materials. (a) Stress–strain curves of VeroClear at different temperatures, which was used to print the SMP active hinges. (b) Failure strain and Young's modulus of VeroClear at different temperatures. (c) Stress–strain curves of the elastomeric materials at room temperature, which were used to print the flexible hinges. (d) Young's modulus of the elastomeric digital materials at room temperature.

2.4. Shape memory behavior of the 4D printed structures

Thermal programming and actuating a SMP include four typical thermomechanical steps. For this purpose, we need to: (i) deform the SMP at a temperature higher than the phase transition temperature (T_{trans}), e.g. glass transition temperature (T_g) in the cross-linked thermosets, (ii) decrease the temperature below T_{trans} while maintaining the external load, (iii) remove the external load at a low temperature to achieve a fixed temporary shape, (iv) increase the temperature above T_{trans} again to trigger the free recovery [28–34].

Details of the thermomechanical programming and actuating of the assembled morphing wing flap with the active SMP hinges are shown in figure 5. In figure 5(a), θ_{max} shows the angle between the moving and stationary parts of the as-fabricated morphing wing flap. For all the morphing flap samples tested, θ_{max} was 70°. We applied a voltage of 12.7 V m^{-1} to the resistive wires for 15 s, which increases the temperature on the surface of the active hinge to 68 °C as shown by finite element simulations and experimental measurements presented in section 4.1. Then, we left a 200 g weight on the moving part of the flap for 3 min, as shown in figure 5(b). This allowed us to program the as-printed bent active hinge into a straight one (figure 5(c)). When the 200 g was removed, the moving part of the flap slightly recovered. In figure 5(c), $\Delta\theta$ indicates the bounce back angle after unloading. The middle flexible hinge followed the same deformation as the active hinge, and stored elastic strain energy, that is released in the recovery process to increase the recovery force.

In the recovery step, the same voltage as the programming step (12.7 V m^{-1} for 15 s) was applied again to the resistive wires, and the active hinges deformed from the flat shape to the bent original shape (Movie S1 is available online at stacks.iop.org/SMS/27/065027/mmedia shows the actuation step of the morphing wing flap). In figure 5(d), θ_{60s} is the recovery angle 60 s after the voltage was applied, which is slightly lower than θ_{max}. θ_{60s} and $\Delta\theta$ were measured accurately for a variety of samples with flexible hinges printed from different elastomeric digital materials, and used in section 4 to calculate the magnitude of recovery ratio and shape fixity.

A similar process was followed to program and actuate the deployable structure. Figure 6(a) demonstrates a 3D printed deployable structure that was programmed into a temporary compact shape through Joule heating and applying a mechanical load. Figure 6 shows the actuation over time of the printed deployable structure (Movie S2 records the recovery process). This structure has the potential to be used as an extensional stage, which can be compacted and extended in one direction. However, the multimaterial inkjet printing technology that we use also enables the fabrication of the two flexible hinges from various elastomers having different stiffnesses. This results in the rotational deformation in addition to the extensional one.

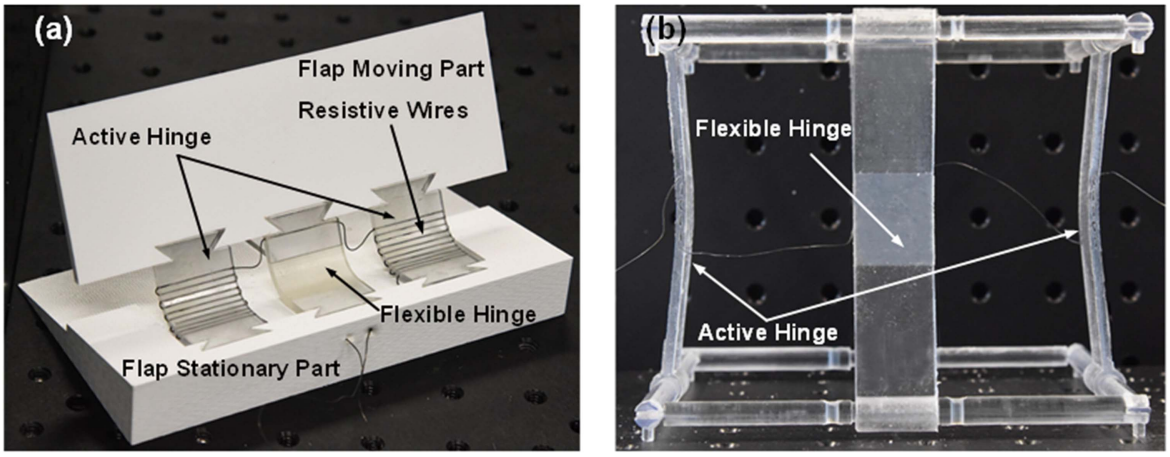

Figure 4. As-fabricated configuration of the 4D printed structures. (a) Morphing wing flap including stationary and moving rigid parts, printed from a thermoplastic (ASA), which were joined together using two active hinges, printed from a SMP (VeroClear), and a flexible hinge whose middle section was from a digital material (mixture of VeroClear and Agilus30) and end sections from VeroClear. (b) Deployable structure comprised of two active hinges printed from VeorClear, and two flexible hinges whose middle section was from a digital material and end sections from VeroClear.

A key desire in the application of the SMP actuators is to enhance their actuation force and load-bearing capacity. In order to assess the effect of the stiffness of the flexible hinges on the load-bearing capacity of the printed structures, we designed a series of experiments by applying an external load during the recovery step. To this end, we hung a 10 g load to the tip of the moving part of the morphing wing flap. Similarly, we left a 50 g on the deployable structure. The active hinges for both structures were printed from VeroClear, while the middle section of the flexible hinges was printed from Agilus30 and FLX9995, which have Young's moduli of $E = 0.43$ MPa and $E = 14.8$ MPa, according to the characterization data shown in figure 3(d). The total weight of the three hinges of the morphing wing flap was 14 g, and the four hinges of the deployable structure 29 g.

Figure 7 indicates that the flexible hinges printed from FLX9995 significantly increase the load-bearing capacity of both 4D printed structures, because they have a higher stiffness, and can store a larger strain energy during programming step. For the morphing wing flap, we repeated these experiments with all elastomeric digital materials, from Agilus30 to FLX9995, with and without an external load, then used a FEA based on a multi-branch viscoelastic model to calculate the recovery ratio of the 4D printed structures. We also tested a control sample with two active hinges and no flexible hinge. The results are presented in detail section 4.2.

3. Finite element modeling

3.1. Heat transfer simulation

Shape training and actuating the active hinges of the 4D printed structures were achieved by localized Joule heating, during which the heat flux generated by electrical current in the resistive wires embedded in the hinge holes was transferred to the SMP to increase its temperature. The heat flux generated by Joule heating (q_{Joule}) is applied to the inner surface of each hole within the active hinge. It then moves through the SMP hinge via conduction (q_{Cond}). Part of the transferred heat increases the hinge temperature, and part of it is dissipated into the surrounding environment at the boundary between the hinge and air through convection (q_{Conv}). Time-dependent 3D temperature distribution in the SMP is governed by the following partial differential equation [35]:

$$\alpha \nabla^2 T = \alpha \left(\frac{\partial^2 T}{\partial x^2} + \frac{\partial^2 T}{\partial y^2} + \frac{\partial^2 T}{\partial z^2} \right) = \frac{\partial T}{\partial t}, \qquad (1)$$

where α is thermal diffusivity, indicating the rate of heat transfer from the high temperature side of the material to the low temperature side, i.e. from the hinge inner surface to the outer surface. The Joule heat flux (q_{Joule}) applied to the hole inner surface as well as the heat flux dissipated from the hinge free surface via convection (q_{Conv}) are considered as the boundary conditions to solve equation (1). This equation with the mentioned boundary conditions has no analytical solution for the geometry of the active hinges described in figure 1. Therefore, finite element simulations were utilized to calculate temperature distributions in the active hinges during Joule heating. To this end, a coupled thermal-electrical analysis was performed in the commercial finite element package ABAQUS (Simulia, Providence, RI, USA). Only a repeating unit cell of the SMP active hinge was modeled to reduce computational expense. Both the resistive wire and the SMP were modeled using elements DC3D8E featuring eight-node linear coupled thermal-electrical brick elements.

Thermal and electrical properties of the resistive wire and the SMP were used in the finite element model to simulate heat transfer. The 0.4 mm diameter resistive wire had an electrical resistivity of $490 \times 10^{-9}\ \Omega\,\text{m}$. Natural convection with the coefficient of heat convection $h = 10\ \text{W m}^{-2}\,\text{K}^{-1}$ [36] was applied at the free surface of the hinge. Density, specific heat, and thermal conductivity of the resistive wire were $8900\ \text{kg m}^{-3}$, $390\ \text{J K}^{-1}$, and $19.5\ \text{W m}^{-1}\,\text{K}^{-1}$, respectively. The values of these parameters for the SMP were $1190\ \text{kg m}^{-3}$, $1470\ \text{J K}^{-1}$, $0.2\ \text{W m}^{-1}\,\text{K}^{-1}$, respectively.

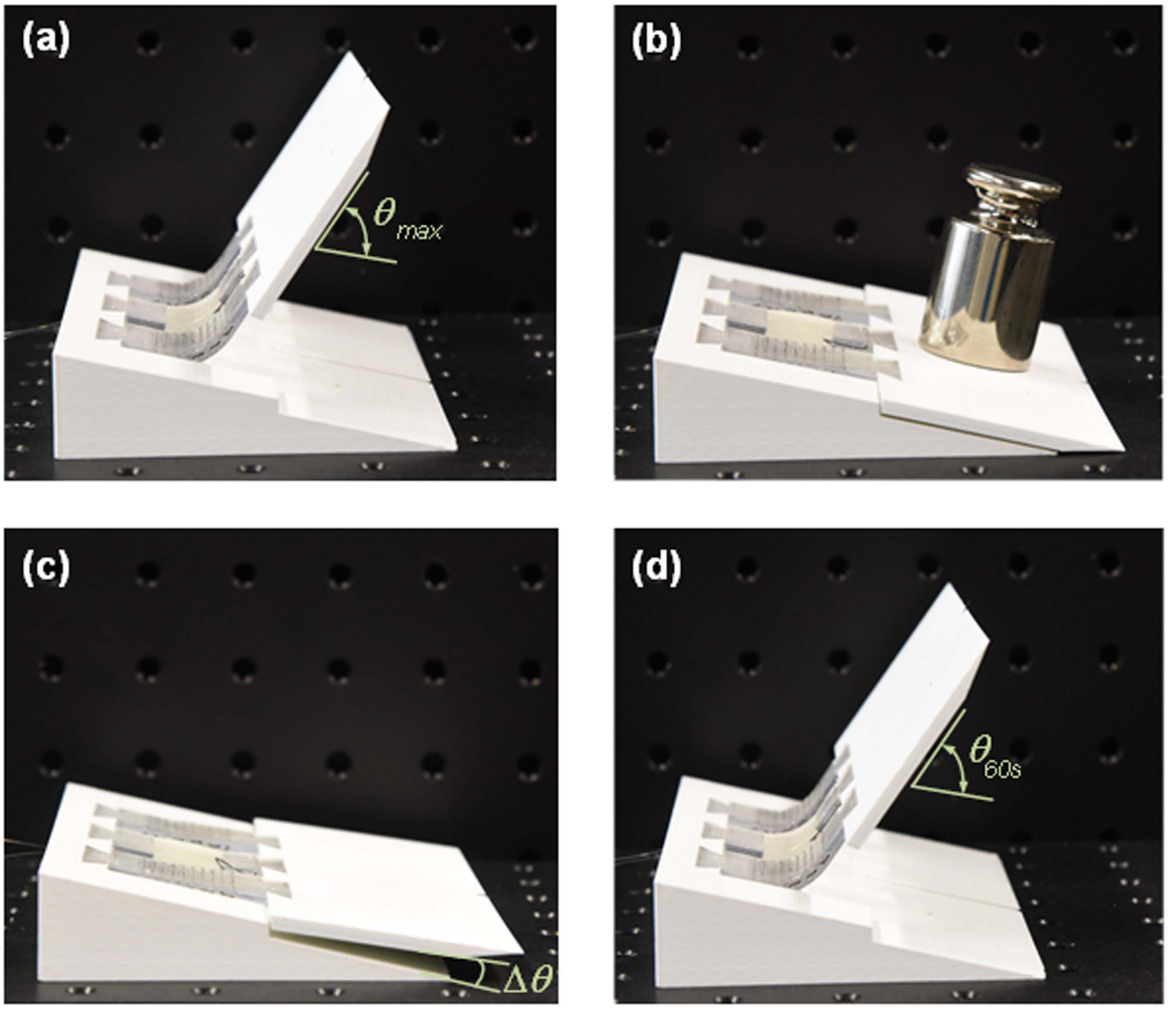

Figure 5. Programming and actuating steps of the morphing wing flap. (a) In the programming process, a voltage of 12.7 V is applied for 15 s. (b) After voltage was disconnected, a 200 g weight was left on the moving part to fix the hinge in the programmed (flat) shape. (c) After 3 min, the weight was removed. The flap remained stable in the new programmed shape. (d) The recovered shape of the hinge 60 s after the voltage was applied to the embedded wire.

3.2. Shape recovery simulation

Detailed FEA simulations were also conducted to model the entire programming and activation steps, and capture time and temperature dependent large deformation of the morphing wing flap. To this aim, we used a multi-branch viscoelastic constitutive model [18, 32, 37] to simulate the shape memory behavior of the morphing wing flap. The FEA simulations were performed using the FEA software ABAQUS with the user-defined constitutive model implemented into a user material (UMAT) subroutine. The material parameters for VeroClear used in the simulations were obtained from previous works [15, 16, 32].

In order to accurately simulate the shape recovery behavior of the morphing flap, the four steps used to program and actuate the flap were modeled following the steps illustrated in figure 5. First, the active hinges were heated up to 68 °C to model the Joule heating step (figure 5(a)). Then a small bending moment was applied to the flap tip to mimic the programming step, which was realized in practice by leaving a 200 g weight on the flap (figure 5(b)). It was found that he magnitude of the bending moment had negligible effect on the stress and strain state of the hinge in the programmed straight shape. In the next step, the active hinge temperature was reduced to 25 °C, then the bending load was removed. As a result, the flap slightly recovered (figure 5(c)). Finally, the temperature of the active hinges was increased again to 68 °C to simulate the recovery step (figure 5(d)). The recovery angles after programming and activating steps (figures 5(c) and (d)) were measured using the developed finite element model, and were compared with the experimental data in section 4.2.

4. Results

4.1. Temperature distribution in the active hinges

The coupled thermal-electrical finite element model described in section in 3.1. was used to model heat transfer in a unit cell of the active hinge, shown in figure 8(a). Figure 8(b) shows the contours of temperature distributions within the hinge unit cell at different times. At $t = 0$, A voltage of 12.7 V m^{-1}

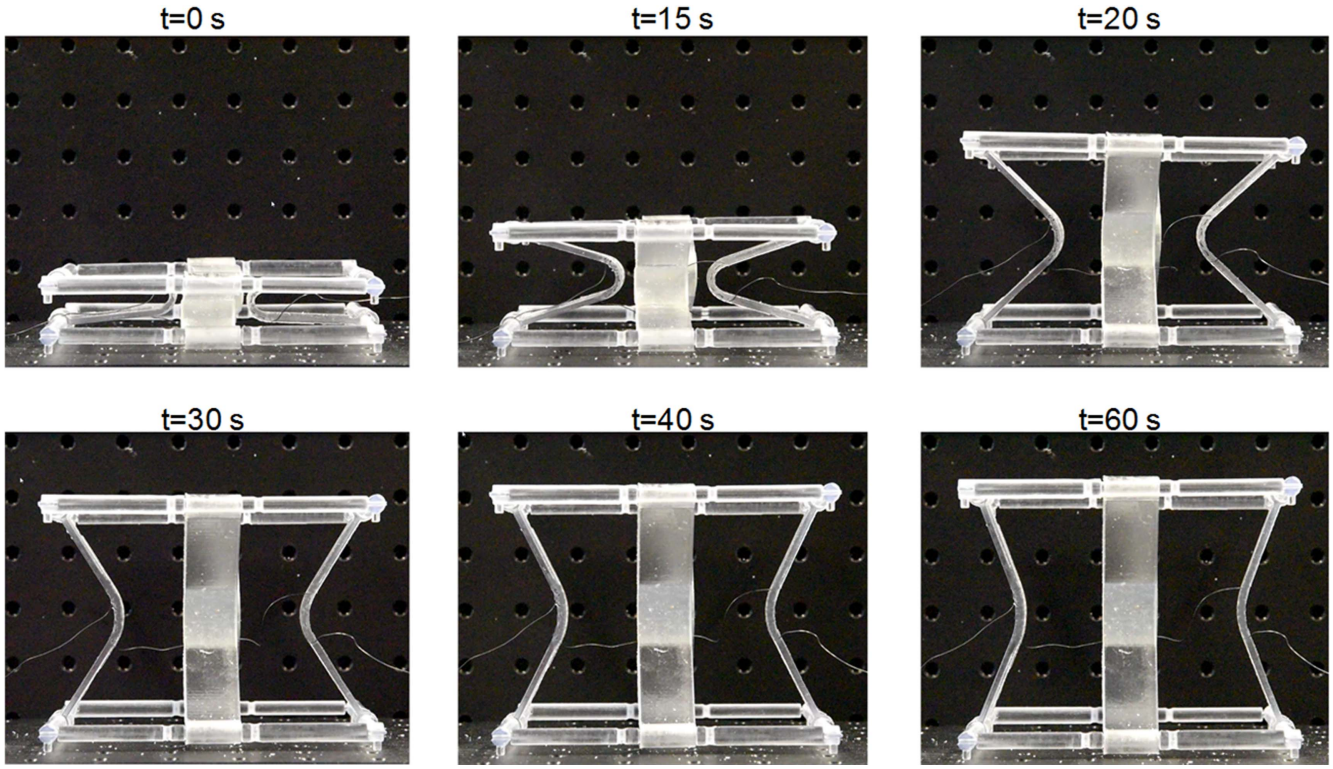

Figure 6. Snapshots of actuation process of the deployable structure comprised of two active hinges and two flexible hinges.

(volts per unit length of the wire) was applied. By applying the voltage, the thermal energy is transferred from the wire outer surface to the inner surfaces of the holes, and the temperature of the SMP active hinge starts to increase. At $t = 15$ s, the voltage was disconnected. Five seconds after voltage disconnection ($t = 20$ s), the temperature distribution became quite uniform in the hinge.

To verify the finite element model, the thermal multimeter with the integrated infrared camera was used to measure the temperature on the free surface of the active hinges. Figure 8(c) compares numerical and experimental results of temperature distribution on the hinge outer surface (Point A in figure 8(a)) upon applying voltage of 12.7 V m^{-1} for 15 s.

Joule heating in the active materials is often modeled using a thermal analysis, i.e. by applying temperature or heat flux directly to the finite element model [38–40]. In the present study, besides thermal-electrical analysis, finite element simulation was also conducted using a thermal analysis, in which the resistive wire was not modeled; instead the heat flux generated in the wire was directly applied to the inner surfaces of the holes as a boundary condition. In this thermal analysis, the SMP active hinge was modeled using eight-node linear brick elements (type DC3D8). Figure 8(c) shows that the thermal-electrical analysis has good agreement with the experimental data, while thermal analysis overestimates temperature, simply because it ignores the time required to heat up the wire. Also, part of the heat is used to increase the wire temperature itself. Since the thermal-electrical analysis estimates the temperature distribution in the active hinge more accurately, it was used to investigate the effect of different parameters such as convection coefficient on temperature distribution in the active hinge.

To study the temperature change of the hinge with time more closely, temperatures on the inner and outer surfaces of the active hinge (Points A and B in figure 8(a)) were extracted and plotted in figure 8(d). Two important trends can be observed. First, the temperature on the inner surface increases much faster than the outer surface. This results in a non-uniform temperature distribution in the active hinge before $t = 20$ s, with the maximum temperature difference between the inner and outer surfaces being 25 °C at $t = 15$ s. It is simply because the inner surface is closer to the heat source, while the outer surface is at the vicinity of the ambient temperature. The heat flux generated by the resistive wire first heats the inner surface of the hole, then is transferred to the outer surface via conduction, and dissipated via convection to the ambient environment.

Shape recovery will not start until the temperature on the outer surface of the unit cell is also high enough. Therefore, temperature on the outer surface dominates the shape recovery. The second important result from figure 8(d) is that, although after voltage disconnection the temperature increases on the outer surface due the heat flux from the hotter inner surface to the colder outer surface, temperature on the inner surface drops immediately at $t = 15$ s. For this reason, after $t = 15$ s the temperature difference decays rapidly, and almost vanishes after $t = 20$ s.

On the free surface of the hinge, the heat is dissipated through convection. In natural (free) convection, the air molecules in contact with the hinge hot surface separate and scatter, causing the air at the vicinity of the hinge surface to

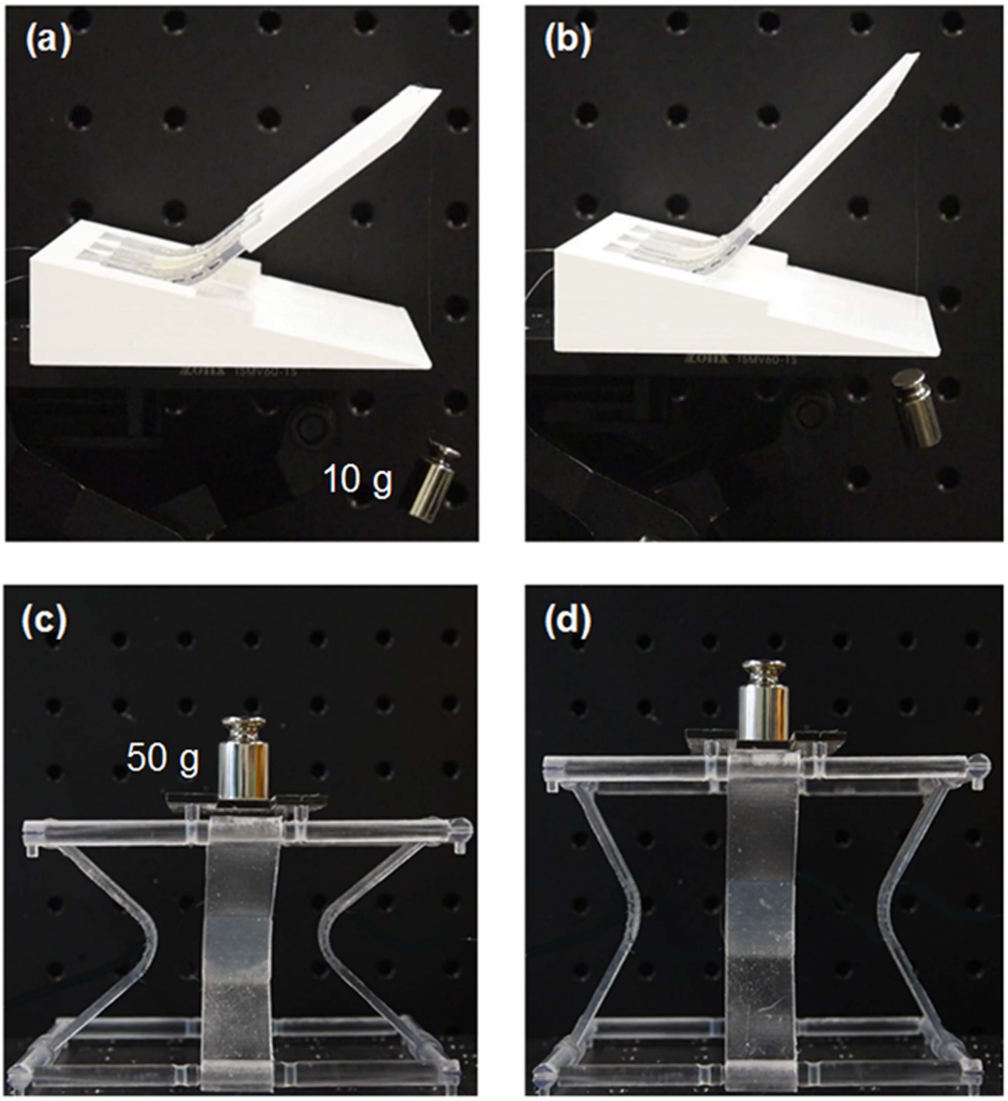

Figure 7. Effect of the stiffness of the flexible hinges on the load-bearing capacity of the 4D printed structures. (a), (b) Recovered shapes of the morphing wing flap with the flexible hinges printed from Agilus30 and FLX9995, respectively. A 10 g weight was hung from the tip of the moving part. (c), (d) Recovered shapes of the deployable structure with the flexible hinges printed from Agilus30 and FLX9995, respectively. A 50 g weight was placed on the actuator.

be less dense. Consequently, the air is displaced and replaced with cooler air, and this way heat transfer between the hinge surface and the surrounding air continues. The experiments of this study were all conducted under natural convection.

In contrast to natural convection, in forced convection the surrounding air is forced to flow over the surface, e.g. using fans. This increases the heat transfer, because it generates an artificially induced convection current. When the morphing wing flap is in operation, e.g. in a flying unmanned aerial vehicle (UAV), the forced convection increases heat dissipation. Assuming a maximum speed of $15\,\mathrm{m\,s^{-1}}$ for the flying UAV, the convection coefficient will be $h = 50\,\mathrm{W\,m^{-2}\,K^{-1}}$, much higher than $h = 10\,\mathrm{W\,m^{-2}\,K^{-1}}$ for natural convection [36]. Figure 8(e) shows the effect of the forced convection on the temperature distribution in the inner and outer surfaces of the active hinge. The forced convection had negligible effect on the maximum temperature on the inner surface, simply because this surface is not in direct contact with the surrounding air. However, as shown figure 8(e), the forced convection reduces the maximum temperature on the outer surface by 10 °C. This necessitates applying a larger actuation voltage or applying the same voltage for a longer time to achieve the required actuation temperature.

The recovery of the SMP is dominated by two factors: heat transfer and material intrinsic recovery. A faster heat transfer can be achieved by the increase of the applied voltage. To assess the effect of the voltage on heat transfer, we defined the heating time as the time at which the temperature at Point A on the outer surface reaches a target temperature of 68 °C. Figure 8(f) shows that as the applied voltage increases, the heating time reduces rapidly, then converges to an extreme value of approximately 7 s.

A practical parameter limiting the maximum voltage is ampacity, i.e. the maximum electrical current the wire can carry before burning. Ampacity is an important parameter that

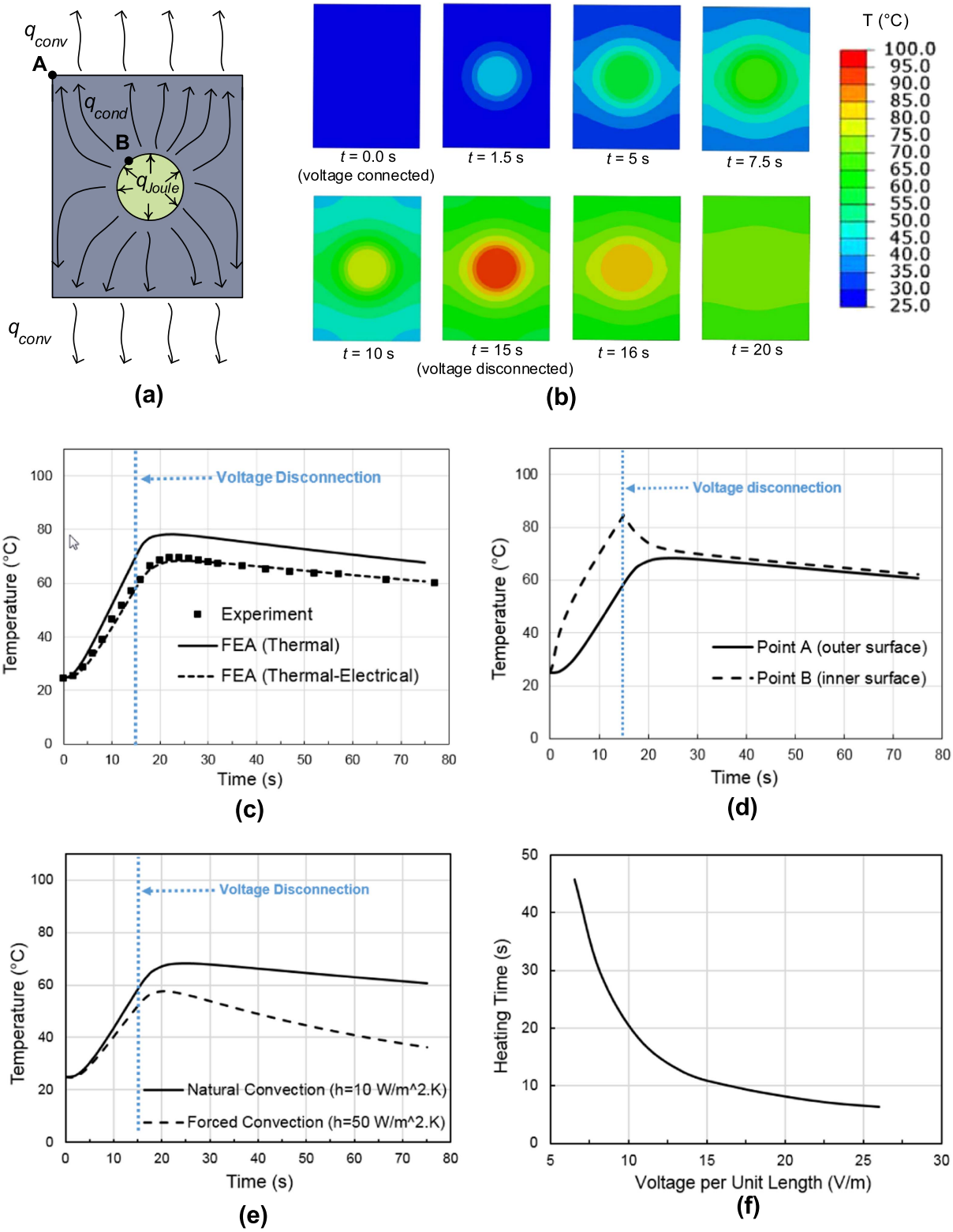

Figure 8. Results of heat transfer simulation in the active hinge. A voltage of 12.7 V m^{-1} (voltage per unit length of the wire) was applied for 15 s. (a) A repeating unit cell of the active hinge representing heat transfer mechanisms, including conduction and convection. (b) Temperature change in the representative unit cell over time. (c) Experimental measurements and FEM predictions of temperature change on the outer surface (Point A of (a)). (d) Comparison of temperature distribution on the outer surface (Point A in (a)) and the inner surface (Point B in (a)). (e) Effect of the natural and forced convections on temperature distribution on the outer surface (Point A in (a)). (f) The heating time versus applied voltage. The heating time is taken as when point A in the representative unit cell (a) reaches the target temperature of 68 °C.

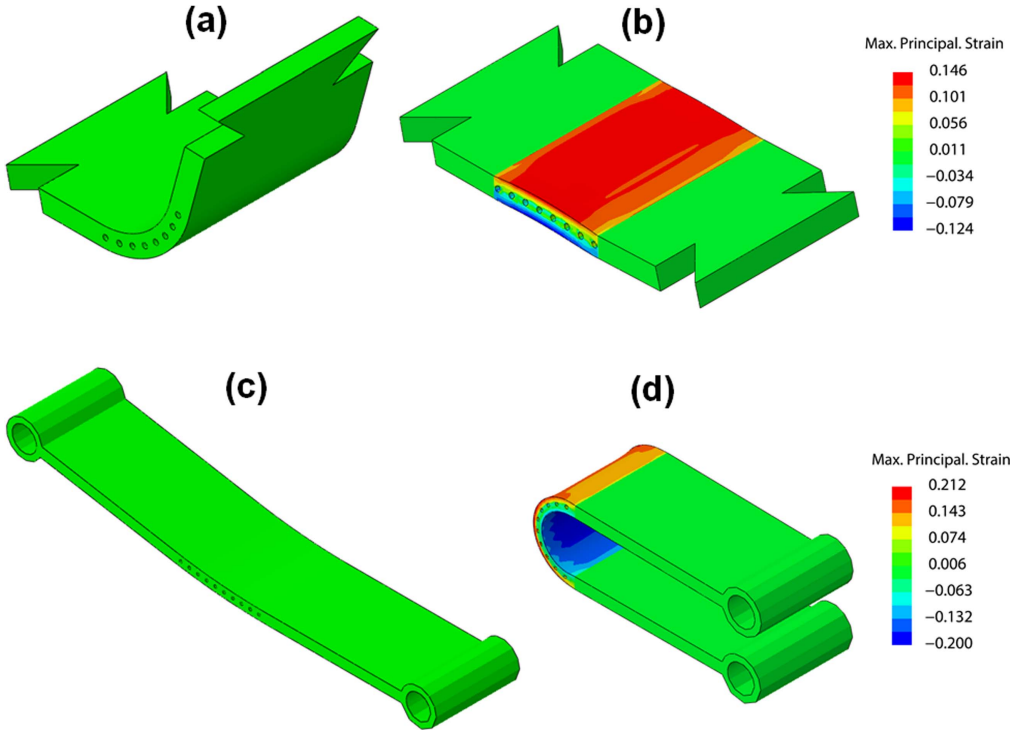

Figure 9. Strain contours in the active hinges (a), (b) as-printed and programmed active hinge used in the morphing wing flap. (c), (d) As-printed and programmed active hinge used in the deployable structure.

needs to be considered, because the electrical current increases almost linearly with voltage. The ampacity of the wire used in this study was 5 A, equivalent to a voltage of approximately 17 V m^{-1}. For this voltage, a heating time of almost 10 s could be achieved according to figure 8(f).

4.2. Shape recovery behavior

The material selection for active and flexible hinges was based on the local strain distribution from FEA simulations of section 3.2. and the experimental data of failure strain from the characterization tests (figure 3(a)). As presented in figure 9, the FEA simulations show the strain contours of the as-printed and programmed active hinges used to fabricate the structures of figure 1. The highest principal engineering strain on the active hinges of the morphing wing flap and the deployable structure were about 14.6% and 21.2%, respectively, which are lower than the failure strain of VeroClear at the programming and actuating temperature (68 °C). Therefore, all the active hinges were printed from VeroClear.

The implemented multi-branch viscoelastic model was used to simulate the shape memory behavior of the morphing wing flap. Figure 10 demonstrates the morphing wing flap configurations during a typical thermomechanical programming and recovery cycle obtained from the finite element simulations. Comparison with the experimental observations shows that the model is able to predict the deformation of the structure in each step with good accuracy. Movie S3 shows the structure deformation during a full cycle of programming and actuating.

To characterize the shape memory of a SMP, we use the shape fixing ratio (R_f) to measure its ability to fix a temporary shape, and the shape recovery ratio (R_r) to measure its ability to recover its original shape upon heating. Specifically, for this shape memory morphing wing flap, we calculate R_f and R_r using the following two equations:

$$R_f = (\theta_{max} - \Delta\theta)/\theta_{max} \text{ and } R_r = 1 - \theta_{60s}/(\theta_{max} - \Delta\theta), \quad (2)$$

where θ_{60s}, θ_{max} and $\Delta\theta$ are defined in figure 5. θ_{max} denotes the angle between the stationary and moving parts of the as-fabricated flap, $\Delta\theta$ is the bounce back angle after unloading at low temperature, and θ_{60s} measures the recovery angle after applying the voltage for 60 s. We used the FEA simulations to investigate the fixity and recovery of the morphing wing flap with flexible hinges whose middle sections were printed from different elastomeric digital materials. We also studied the load-bearing capacity of the morphing wing flap by applying an external load to the moving part.

Figure 11 shows the recovery ratio and shape fixity of the morphing wing flap with flexible hinges printed from various digital materials exhibiting different stiffnesses (figure 3(d)), which were measured experimentally and compared with the finite element predictions. In figures 11(a) and (c), the weight of the moving part of the flap (15 g) was the only applied load, while in figures 11(b) and (d), a 10 g load was also hung at the end of the flap, as shown in figures 7(a), (b). The horizontal axis on figure 11 shows the Young's modulus of the elastomeric digital material used to print the flexible hinges. It starts with a value of zero ($E = 0$) on the origin,

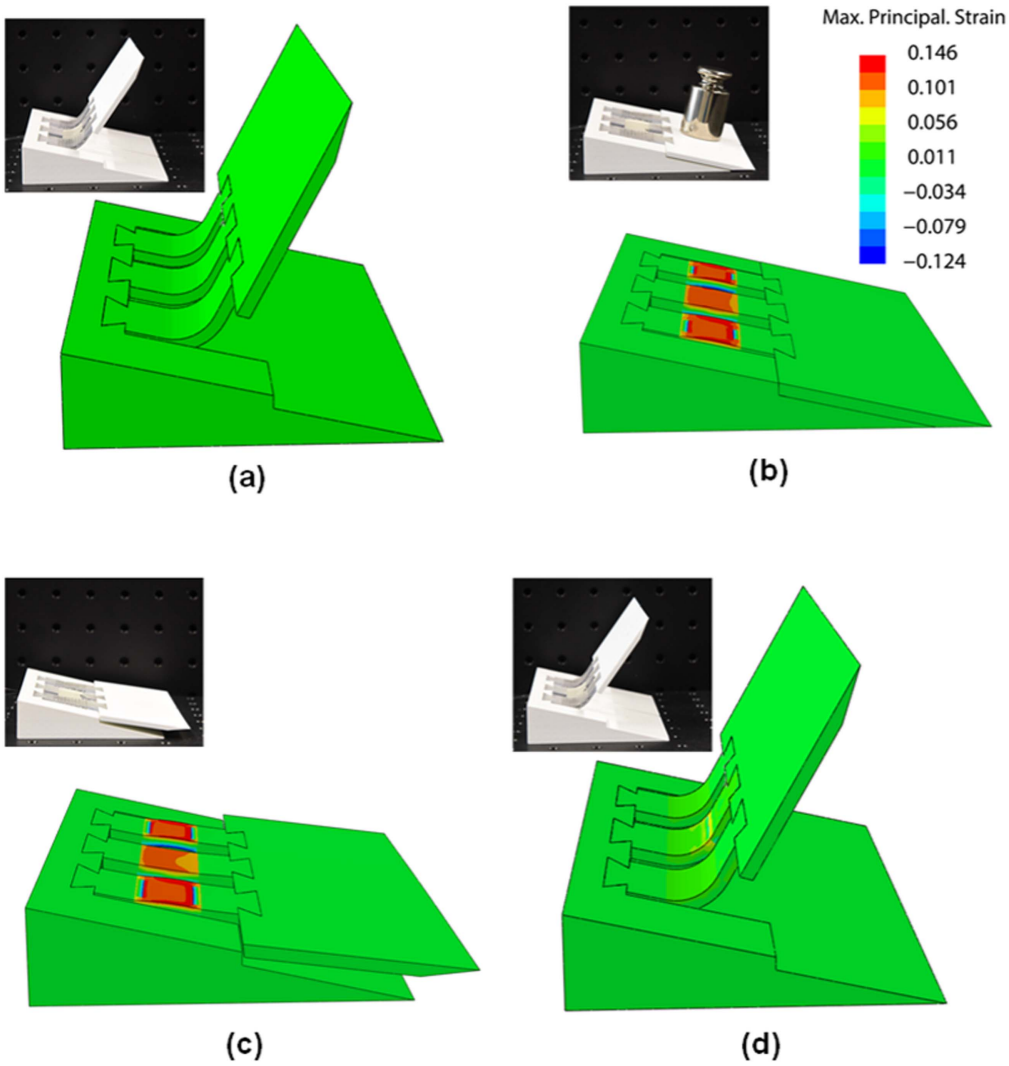

Figure 10. Finite element predictions of the morphing wing flap configurations during programming and actuating steps. The insets are from figure 5 for comparison purposes. (a) Initial configuration of the flap. (b) Deformed shape of the flap under a combination of the mechanical and thermal loads. (c) Programmed shape of the flap at $T < T_g$. (d) Recovered shape of the flap at $T > T_g$.

corresponding with a control sample that does not contain any flexible hinge.

Figure 11 shows that the FEA simulations are able to reproduce the recovery ratio and shape fixity of the morphing wing flap with reasonable accuracy. It confirms that the use of a flexible hinge can significantly increase the recovery ratio of the morphing wing flap. For example, in the case where no external load is applied, and no flexible hinge is used, the recovery ratio is only about 0.86. In comparison, the use of a flexible hinge, printed from FLX9995 with Young's modulus of 14.8 MPa, increases the recovery ratio to 0.97, confirming the enhanced actuation performance which is a necessity for the active structures. This effect is even more significant when an external load is applied. For instance, when a 10 g load is hung at the tip of the flap (figures 7(a), (b)), FLX9995 flexible hinge increases the recovery ratio from 0.75 to 0.94.

On the other hand, figures 10(c), (d) show that the use of stiffer materials to print the flexible hinges reduces the shape fixity, because the stiffer hinges store a larger elastic energy in the programming step, and tend to create a larger bounce back angle. However, all the specimens printed with different digital materials were able to realize a shape fixity of at least 95%.

These results show that the multimaterial inkjet 3D printing technology provides high tailorability of the mechanical properties of the flexible hinges to control fixity and recovery of the printed active structures, thus allowing remarkable design flexibility. The good agreement between the finite element simulations and experimental results confirms that the developed multi-branch model can be used to design sophisticated 4D printed structures undergoing complex large deformations.

The abovementioned structures show that incorporation of active and flexible hinges into fully 3D printed parts is able to generate 3D shapes. More complex shapes can be accomplished by rearrangement of active and passive segments to achieve desired functionality. Besides, the 4D printed active structures presented here exhibited pure bending or extensional deformation. A combination of these deformations can be achieved by utilizing the flexibility of

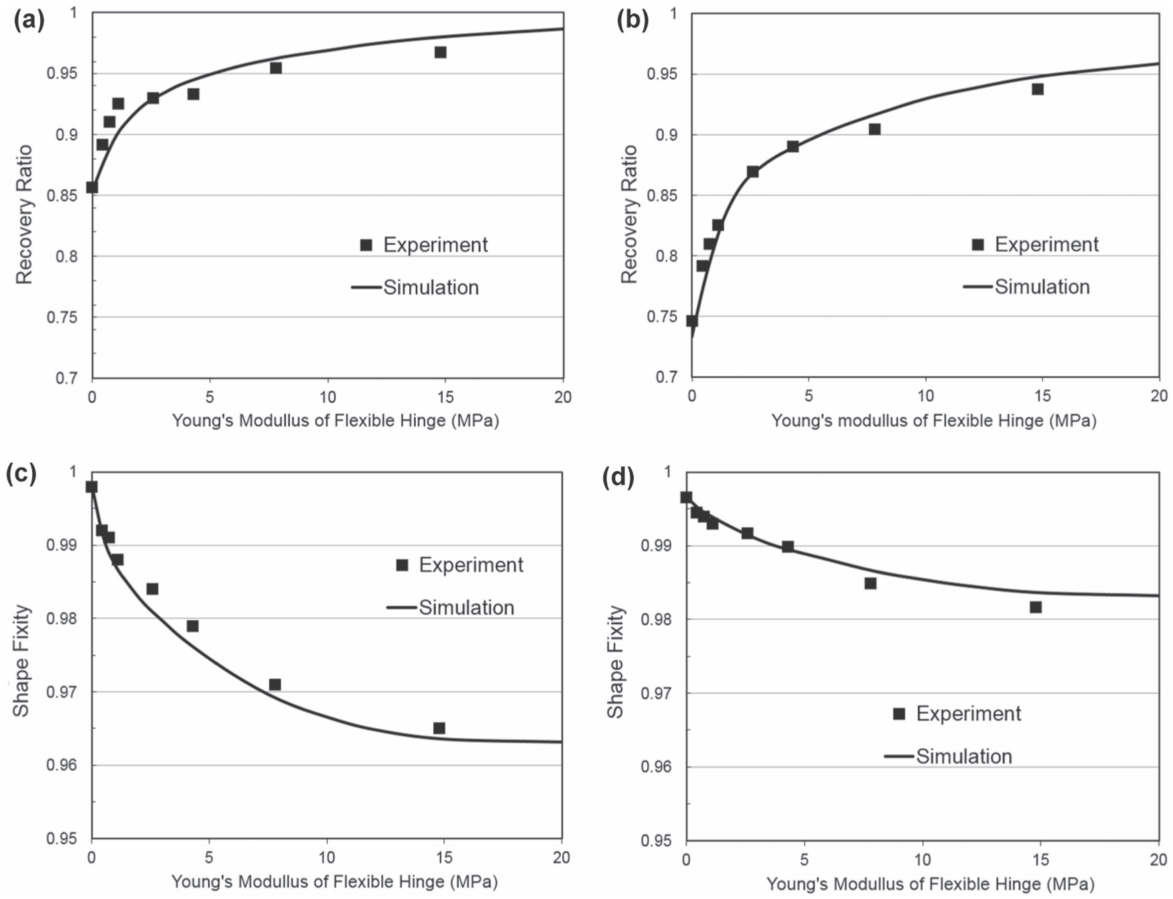

Figure 11. Experimental measurements and finite element predictions of the shape memory and shape fixity of the morphing wing flap with flexible hinges printed from various elastomeric digital materials, from Agilus30 to FLX9995. One control sample was tested with no flexible hinge. (a), (b) Recovery ratio of the morphing wing flap with no external load, and with a 10 g external load, respectively. (c), (d) Shape fixity of the morphing wing flap with no external load, and with a 10 g external load, respectively.

multimaterial 3D printing to combine the basic designs used here.

5. Conclusions

4D printing has potential applications for low cost and rapid production of self-actuating mechanisms. However, it is important to develop novel approaches to increase the actuation force, which is crucial for 4D printed structures. In this study, we showed that the combined use of the active and flexible hinges is an effective approach to increase the recovery ratio and the load-bearing capacity of the 4D printed structures. We demonstrated actuation of two types of 4D printed structures, a morphing wing flap and a deployable structure, realized by thermal actuation of the active hinges that were 3D printed from a SMP to connect rigid (non-active) parts of the structures. Additional flexible hinges printed from an elastomeric digital material were used to enhance recovery force during actuation.

The load-bearing capacity of the printed structures depend on the stiffness of the flexible hinges. We were able to generate a range of recovery ratios and shape fixities for the morphing wing flap by using flexile hinges printed from elastomeric digital materials with various stiffnesses. A viscoelastic multi-branch model incorporated into a finite element model was able to simulate the thermomechanical behavior of the 4D printed morphing wing flap, and accurately predict its shape fixity and recovery ratio. Thus, the model can be used to design complex active structures for specific performance and deformation, and help select the materials with appropriate thermomechanical properties, while reducing the time and expense required for experimentation.

Along with enhanced actuation, the new 4D printed structures demonstrate the effectiveness of the inexpensive localized Joule heating based on resistive wires. An important aspect of thermal actuation by Joule heating is management of temperature distribution within the active material to ensure it remains in a certain limit, as the failure strain of the SMP rapidly decays with temperature. To improve heating efficiency, a coupled thermal-electrical FEA was performed to study the effect of different parameters on temperature distribution. The model was verified with the experimental temperature data, and was used to investigate the effect of the applied voltage, heating time, and heat dissipation through convection on the temperature distribution in the active hinges.

Acknowledgments

SA and QG gratefully acknowledge financial support from NAMIC@NTUitive on the project of 3D and 4D Printing Technologies to Create Actuating and Transforming Components. The authors also acknowledge the support by the SUTD Digital Manufacturing and Design Centre (DManD), funded by the Singapore National Research Foundation. QG acknowledges the SUTD Start-up Research Grant.

ORCID iDs

Qi Ge https://orcid.org/0000-0002-3548-547X

References

[1] Truby R L and Lewis J A 2016 Printing soft matter in three dimensions *Nature* **540** 371–8
[2] Ventola C L 2014 Medical applications for 3D printing: current and projected uses *Pharmacy Ther.* **39** 704
[3] Zolfagharian A, Kouzani A Z, Khoo S Y, Moghadam A A A, Gibson I and Kaynak A 2016 Evolution of 3D printed soft actuators *Sensors Actuators* A **250** 258–72
[4] Bartlett N W, Tolley M T, Overvelde J T, Weaver J C, Mosadegh B, Bertoldi K, Whitesides G M and Wood R J 2015 A 3D-printed, functionally graded soft robot powered by combustion *Science* **349** 161–5
[5] Slyper R and Hodgins J 2012 Prototyping robot appearance, movement, and interactions using flexible 3d printing and air pressure sensors *2012 IEEE RO-MAN* (Piscataway, NJ: IEEE) pp 6–11
[6] Umedachi T, Vikas V and Trimmer B A 2013 Highly deformable 3D printed soft robot generating inching and crawling locomotions with variable friction legs *2013 IEEE/RSJ Int. Conf. on Intelligent Robots and Systems (IROS)* (Piscataway, NJ: IEEE) pp 4590–5
[7] Joshi S C and Sheikh A A 2015 3D printing in aerospace and its long-term sustainability *Virtual Phys. Prototyping* **10** 175–85
[8] Castro N J, Meinert C, Levett P and Hutmacher D W 2017 Current developments in multifunctional smart materials for 3D/4D bioprinting *Curr. Opin. Biomed. Eng.* **2** 67–75
[9] Ge Q, Qi H J and Dunn M L 2013 Active materials by four-dimension printing *Appl. Phys. Lett.* **103** 131901
[10] Khoo Z X, Teoh J E M, Liu Y, Chua C K, Yang S, An J, Leong K F and Yeong W Y 2015 3D printing of smart materials: a review on recent progresses in 4D printing *Virtual Phys. Prototyping* **10** 103–22
[11] Leist S K and Zhou J 2016 Current status of 4D printing technology and the potential of light-reactive smart materials as 4D printable materials *Virtual Phys. Prototyping* **11** 249–62
[12] Momeni F, Liu X and Ni J 2017 A review of 4D printing *Mater. Des.* **122** 42–79
[13] Tibbits S 2014 4D printing: multi-material shape change *Archit. Des.* **84** 116–21
[14] Ding Z, Yuan C, Peng X, Wang T, Qi H J and Dunn M L 2017 Direct 4D printing via active composite materials *Sci. Adv.* **3** e1602890
[15] Ge Q, Dunn C K, Qi H J and Dunn M L 2014 Active origami by 4D printing *Smart Mater. Struct.* **23** 094007
[16] Ge Q, Sakhaei A H, Lee H, Dunn C K, Fang N X and Dunn M L 2016 Multimaterial 4D printing with tailorable shape memory polymers *Sci. Rep.* **6** 31110
[17] Mao Y, Ding Z, Yuan C, Ai S, Isakov M, Wu J, Wang T, Dunn M L and Qi H J 2016 3D printed reversible shape changing components with stimuli responsive materials *Sci. Rep.* **6** 24761
[18] Mao Y, Yu K, Isakov M S, Wu J, Dunn M L and Qi H J 2015 Sequential self-folding structures by 3D printed digital shape memory polymers *Sci. Rep.* **5** 13616
[19] Rodriguez J N, Zhu C, Duoss E B, Wilson T S, Spadaccini C M and Lewicki J P 2016 Shape-morphing composites with designed micro-architectures *Sci. Rep.* **6** 27933
[20] Teoh J, An J, Chua C, Lv M, Krishnasamy V and Liu Y 2017 Hierarchically self-morphing structure through 4D printing *Virtual Phys. Prototyping* **12** 61–8
[21] Cantrell J and Ifju P 2015 Experimental characterization of unimorph shape memory polymer actuators incorporating transverse curvature in the substrate *Exp. Mech.* **55** 1395–409
[22] Zhang C-S and Ni Q-Q 2007 Bending behavior of shape memory polymer based laminates *Compos. Struct.* **78** 153–61
[23] Lan X, Liu Y, Lv H, Wang X, Leng J and Du S 2009 Fiber reinforced shape-memory polymer composite and its application in a deployable hinge *Smart Mater. Struct.* **18** 024002
[24] Liu Y, Gall K, Dunn M L and McCluskey P 2004 Thermomechanics of shape memory polymer nanocomposites *Mech. Mater.* **36** 929–40
[25] Lagakos N, Jarzynski J, Cole J and Bucaro J 1986 Frequency and temperature dependence of elastic moduli of polymers *J. Appl. Phys.* **59** 4017–31
[26] Jin Z, Pramoda K, Xu G and Goh S H 2001 Dynamic mechanical behavior of melt-processed multi-walled carbon nanotube/poly (methyl methacrylate) composites *Chem. Phys. Lett.* **337** 43–7
[27] Liu Y, Gall K, Dunn M L, Greenberg A R and Diani J 2006 Thermomechanics of shape memory polymers: uniaxial experiments and constitutive modeling *Int. J. Plast.* **22** 279–313
[28] Zhao Q, Qi H J and Xie T 2015 Recent progress in shape memory polymer: new behavior, enabling materials, and mechanistic understanding *Prog. Polym. Sci.* **49** 79–120
[29] Beilvert A, Chaubet F, Chaunier L, Guilois S, Pavon-Djavid G, Letourneur D, Meddahi-Pellé A and Lourdin D 2014 Shape-memory starch for resorbable biomedical devices *Carbohydrate Polym.* **99** 242–8
[30] Ge Q, Westbrook K K, Mather P T, Dunn M L and Qi H J 2013 Thermomechanical behavior of a two-way shape memory composite actuator *Smart Mater. Struct.* **22** 055009
[31] Hager M D, Bode S, Weber C and Schubert U S 2015 Shape memory polymers: past, present and future developments *Prog. Polym. Sci.* **49** 3–33
[32] Yu K, Ge Q and Qi H J 2014 Reduced time as a unified parameter determining fixity and free recovery of shape memory polymers *Nat. Commun.* **5** 3066
[33] Tolley M T, Felton S M, Miyashita S, Aukes D, Rus D and Wood R J 2014 Self-folding origami: shape memory composites activated by uniform heating *Smart Mater. Struct.* **23** 094006
[34] Westbrook K K, Mather P T, Parakh V, Dunn M L, Ge Q, Lee B M and Qi H J 2011 Two-way reversible shape memory effects in a free-standing polymer composite *Smart Mater. Struct.* **20** 065010
[35] Incropera F and DeWitt D 1990 *Fundamentals of Heat and Mass Transfer* (New York: Wiley) p A5A, 7
[36] Sartori E 2006 Convection coefficient equations for forced air flow over flat surfaces *Sol. Energy* **80** 1063–71

[37] Westbrook K K, Kao P H, Castro F, Ding Y and Qi H J 2011 A 3D finite deformation constitutive model for amorphous shape memory polymers: a multi-branch modeling approach for nonequilibrium relaxation processes *Mech. Mater.* **43** 853–69

[38] Yu K, Westbrook K K, Kao P H, Leng J and Qi H J 2013 Design considerations for shape memory polymer composites with magnetic particles *J. Compos. Mater.* **47** 51–63

[39] Zhou G, Zhang H, Xu S, Gui X, Wei H, Leng J, Koratkar N and Zhong J 2016 Fast triggering of shape memory polymers using an embedded carbon nanotube sponge network *Sci. Rep.* **6** 24148

[40] Yu C, Duan Z, Yuan P, Li Y, Su Y, Zhang X, Pan Y, Dai L L, Nuzzo R G and Huang Y 2013 Electronically programmable, reversible shape change in two-and three-dimensional hydrogel structures *Adv. Mater.* **25** 1541–6